Advances in Materials Research, *Vol. 13, No. 5 (2024) 391-416*
https://doi.org/10.12989/amr.2024.13.5.391

Experimental and numerical investigation on low-velocity impact behaviour of thin hybrid carbon/aramid composite

Sojan Andrews Zachariah[1,2a], Dayananda Pai K[1b], Padmaraj N H[1c]
and Satish Shenoy Baloor[*1]

*[1]Department of Aeronautical and Automobile Engineering, Manipal Institute of Technology,
Manipal Academy of Higher Education, Manipal, Karnataka 576104, India*
*[2]Department of Operations and Development, Worldwide Oilfield Machine Middle East, P.O. Box 32478,
Dubai, United Arab Emirates*

(*Received August 13, 2023, Revised August 19, 2024, Accepted August 20, 2024*)

Abstract. Hybrid composite materials are widely used in various load-bearing structural components of micro - mini UAVs. However, the design of thin laminates for better impact resistance remains a challenge, despite the strong demand for lightweight structures. This work aims to assess the low-velocity impact (LVI) behaviour of thin quasi-isotropic woven carbon/ aramid epoxy hybrid laminates using experimental and numerical techniques. Drop tower impact test with 10 J and 15 J impact energies is performed on carbon/epoxy laminates having aramid layers at different sequences and locations. The impact behaviour is experimentally evaluated using force-time, force-deformation, and energy-time histories considering delamination threshold load, peak load, and laminate deflection. Ultrasonic C-scan is performed on the post-impact samples to analyse the insidious damage profile at different impact energies. The experimental data is further utilized to numerically simulate LVI behaviour by employing the representative volume element model. The numerical results are in good agreement with the experimental data. Numerical and experimental approach predicts that the hybrid laminates with aramid layers at both impact and non-impact sides of the laminate exhibits significant improvement in the overall impact behaviour by having a subcritical damage morphology compared to carbon/epoxy laminate. A combined numerical-experimental approach is proposed for evaluating the effective impact performance.

Keywords: finite element analysis; hybrid composite; low velocity impact behaviour; micro - mini UAV; representative volume element

1. Introduction

The current trends in the research and development activities of alternative materials for micro/mini Unmanned Aerial Vehicle (UAVs) record a phenomenal growth in polymer-based composite laminates for their various structural applications, like the fuselage and the wing (Verma *et al.* 2018, Denning 2004, Padmaraj *et al.* 2021). Carbon Fibre Reinforced Polymers (CFRP) is a

---

[*] Corresponding author, Professor, E-mail: satish.shenoy@manipal.edu
[a] Ph.D., E-mail: sojanandrews@yahoo.co.in
[b] Professor, E-mail: dayanand.pai@manipal.edu
[c] Associate Professor, E-mail: padmaraj.nh@manipal.edu

http://www.techno-press.org/?journal=amr&subpage=5 ISSN: 2234-0912 (Print), 2234-179X (Online)

promising material for UAV structural application due to their exceptional in-plane mechanical properties and excellent specific strength (Verma *et al.* 2018, Soetanto and Tritjahjono 2016). Nevertheless, the inherent brittle nature of the carbon fibre and epoxy matrix contributes towards low fracture toughness and through-thickness impact performance. In aerospace components, the primary and secondary structures made of CFRP are vulnerable to impact forces in the through-thickness directions (Kumar Jha *et al.* 2019). The impact events are of various kinds and are usually encountered by a structure during various manufacturing, operational, and routine maintenance stages. Impact events encountered by structural components is a dynamic loading scenario generally categorised into low, high, and ballistic impacts. Mini-UAVs with belly landing feature is finding application in tactical and military applications like Bayraktar Mini Unmanned Aerial Vehicle (PS and Jeyan 2020). Weight reduction of structures for the mini-UAVs are of significant importance as the net weight of the UAV only ranges from 1.5-10 kilograms. The average incident velocity during belly landing is 3-10 m/s, which fits the LVI categorisation. The impact energy due to the structural weight of ranging 1.5-10 kilograms are around 5- 20 J and is exclusively based on the UAV type (Condruz *et al.* 2020, Zahran and Abdelwahab 2019). Troiani *et al.* (2015) have studied the enhancement of crash absorbing capability of CFRP suitable for small UAV based on the amount of incident impact energy absorbed (Karahan *et al.* 2019, Karahan and Yildirim 2015, Shaker *et al.* 2017). However, there is a requirement for investigations in LVI impact-resistant thin hybrid composite laminates suitable for mini belly-landing UAV structural applications.

Low-velocity impacts (LVI) create serious safety issues due to the absence of visible and extended damage in the composite structure during routine visual inspections. The damage caused due to LVI is categorised as Barely Visible Impact Damage (BVID). However, BVID is insidious when the structure is put back to service. These LVI damaged structures may undergo a catastrophic failure when they persisted and ignored. Nevertheless, few works identify the LVI as the scenario where the impactor hits the target at an impact velocity of 1-10 m/s; it cannot be concluded without considering other impact parameters, precisely the incident energy and the impactor geometry (Sarasini 2017). The parameter CE, known as the specified ratio of impact energy related to the laminate thickness, can help identify the threshold impact energy of a specific laminate before penetration as per ASTM D7136/D7136M-15. An exciting parameter obtained from the mechanical response of LVI tests and data worth for the design process is the Delamination Threshold Load (DTL). Therefore, the LVI studies should indeed focus on the total effect of the impact scenario while critically analysing the impact performance of a laminate.

Hybridisation is an efficient strategy for imparting impact strength in laminates reinforced with Low Strain Materials (LSM). The two primary hybridisation approaches are inter-ply and intra-ply. The inter-ply approach is the easy and less complicated method in which High Strain Material (HSM) are incorporated layer by layer (Zachariah *et al.* 2021, Zachariah *et al.* 2024, Fotouhi *et al.* 2017). The laminate level property and overall stacking balance are not compromised in the inter-ply approach. The intra-ply approach is comparatively complicated and laborious where the HSM is added at the individual layer, in yarn by yarn or in warp and weft direction. The woven fabric composites that exhibit better balance in the longitudinal and transverse direction are reported to be suitable for impact-resistant laminates when compared to unidirectional (UD) and cross-ply laminates (Naik *et al.* 2000, Soliman *et al.* 2012). Katnam *et al.* (2019) studied the impact damage tolerance of laminates with quasi-unidirectional woven fabric with yarn level S-glass/PP hybrid material. The balance between the in-plane and thickness is deemed mandatory for high-end structural components (Andrews Zachariah *et al.* 2022). Bidirectional (BD) woven carbon composites have been studied by Karahan and Karahan (2014). They concluded on the superiority of BD architecture over UD fabric concerning the impact performance. Materials like glass and basalt, and aramid (Kevlar) are studied by various researchers in the context of hybridization (Yang *et al.* 2017, Priyanka *et al.* 2017, Evci and Gülgeç 2012). High-performance fibres of the para-aramid class are used as protective fabrics because of their high impact resistance. Twaron® equivalent to Kevlar® of DuPont are the extensively reported high-performance fibres. Para-aramid fibre is five times stronger than steel and possesses greater flexibility (Dong and Sun 2009). Huang *et al.* (2021) have studied the impact behaviour of Twaron® under drop tower test. The study reports on its better impact-rate-sensitivity and the greater initial impact energy resulted in a better peak load, greater strain to failure, improved energy absorption and smaller contact duration during the impact process. Alkex® are also a commercially recognised para-aramid which is a trademark product of Hyosung corporation. However, the Alkex® having good toughness and remarkable tenacity is not reported. The influence of para-aramid fabric in imparting impact strength at various magnitudes of impact energies are reported (Vachon *et al.* 2013, Valença *et al.* 2015, Marom *et al.* 1986, Nayak *et al.* 2021). However, the majority of the impact studies are reported in ballistic range and with thick hybrid laminates (Pigazzini *et al.* 2018, Berk *et al.* 2017, Micheli *et al.* 2016). Nevertheless, the impact behaviour mechanism of ballistic or high-performance fabrics under low-velocity impacts on thinner laminates still requires data based on experimental studies; it is crucial for engineering material design and developing para-aramid fabrics with improved all-round impact resistance performance for thin structural components.

Finite Element Analysis (FEA) based numerical simulations are getting greater acceptance in recent design and development activities (Sun and Hallett 2017). The remarkable gain in the efficacy of computational technology has enabled researchers to perform software-based analysis at higher-order compared to the past. Bandaru *et al.* (2018) numerically evaluated the impact response of thermoplastic hybrid composites using the Chang-Channg damage model, and the results were in close compliance with experimental data for the force-time relationship and for the damage profile. Numerical models can predict the damage mechanisms of through-thickness damage during impact loading in thin carbon/epoxy laminates, as reported by Mahmoud *et al.* (2019). Yang *et al.* (2015) numerically validated the LVI on inter-ply hybrid laminates at different impact velocities. They concluded that the progressive failure model developed using the inbuilt ABAQUS -VUMAT subroutine can be utilised for predicting the failure of inter-ply hybrid composites, and the results were matching the experimental data.

However, studies on thin woven hybrid composites with carbon and aramid reinforcements are not widely reported. Hence there is a need for additional information on the correlation between the numerical and the experimental data of hybrid carbon/aramid composites subjected to LVI. Current computational capabilities and advancements in the simulation platforms enable the composite structural analysis at micro, macro, and mesoscale. Microscale homogenisation avoids the disadvantages of carrying experimental values for numerical analysis (Denning 2004, Shi *et al.* 2012). Dixit *et al.* (2013) reported the close compliance of unit cell model analysis for getting the properties of composites for multiscale analysis. The data from unit cell analysis is higher than the actual experimental data because of the warpage of fabrics during fabrication and the loss of properties during the weaving process. In the micro-scale, the Representative Volume Element (RVE) based models are often used with single fibres surrounded by matrix. The fibre volume fraction for RVE is maintained the same as the overall volume fraction of fibres in the lamina (Papakaliatakis and Karalekas 2010, Sørensen 2017). Naghdinasab *et al.* (2018) reported the degradation of material properties in composite RVE caused due to damages. The RVE models are capable of capturing elastic properties of composites that can be homogenised and used for determining laminae properties (Rayhan and Rahman 2020). Based on the literature, RVE based numerical simulation in hybrid composites with multi-moduli fabrics are not extensively reported. There is a substantial gap in the available studies on the comprehensive data on the influence of HSM fabric in CFRP laminates with overall thickness below 3 mm, which are suitable for impact-resistant structural applications in small, micro/mini UAVs (PS and Jeyan 2020).

Hence in this work, an investigation on the LVI behaviour of thin hybrid plain-woven carbon and Alkex® fabric of para-aramid class is carried out to understand the effect of location and stacking sequence of woven aramid layers. The hybrid carbon/aramid laminates for the study is fabricated using the Vacuum Assisted Resin Infusion Method (VARIM) process. The stacking sequence and the number of carbon plies are maintained the same in all the samples as part of the novel approach followed in this study. The experiment focuses on the aspect of enhancing the impact performance of a CFRP with a woven quasi-isotropic layup. Five hybrid laminates were fabricated by incorporating aramid fabrics in CFRP by varying the three aspects of the aramid layer, namely, the number of plies, the stacking sequence, and the ply position. The LVI performance of thin hybrid carbon/aramid epoxy laminate is studied using a drop tower test. The experimental LVI data is numerically validated using ABAQUS-EXPLICIT. Elastic material property used for the simulation is determined from RVE based microscale analysis of the composite unit-cell in ANSYS WORKBENCH using the material designer module. The ultrasonic C-Scan technique is used to analyse the post-impact damage morphology of the specimens (Lin and Waas 2021, Fischer *et al.* 2019). Reinforcements with bidirectional woven architectures are extensively employed for better impact response. This study expects to provide useful and novel insights into the LVI behaviour of thin carbon/aramid epoxy hybrid composites to find wide-ranging applications in micro/mini UAVs. The simulation results presented in this study will provide a better understanding of the failure criteria and modes pertaining to the design aspects while tailoring properties in composite materials.

2. Experimental study

2.1 Specimen preparation

The prospective tests on hybrid carbon/aramid composite laminates are presented in this section. A CFRP laminate and five hybrid laminates with respective laminae location, in the cross-sectional view as detailed in Fig. 1, was investigated for analysing the LVI behaviour. The arrow in Fig. 2 denotes falling direction of the impactor on the laminate. The laminates were fabricated using carbon (3K-BD plain-woven, surface density 200 g/m^2) and aramid (ALKEX® 1500D BD plain-woven, surface density 220 g/m^2) with BhorBond EPCH, a Bisphenol-A based liquid epoxy resin, and low viscosity BhorBond EPCH amine hardener. The reinforcement fabrics were procured from Composite Tomorrow Limited, India and manufactured by Hyosung corporation.

The laminates were fabricated using the Vacuum-Assisted Resin Infusion Moulding (VARIM) technique, in an in-house built fabrication setup (Andrews Zachariah *et al.* 2022). The process parameters were designed as per the data from the literature van Oosterom *et al.* 2019, Hashim *et al.* 2017, Nugroho *et al.* 2018. The tacking sequence implemented in this study was derived from the literature data, where HSM is positioned at the outer faces of the laminate (Yusuff *et al.* 2005, Gustin *et al.* 2005, Bulut and Erkliğ 2018). A quasi-isotropic stacking sequence was used for the carbon layers. The arrangement of the carbon layer was maintained the same in all laminates for the ease of comparison on the stacking and position of the hybrid inter-ply layer. The physical properties

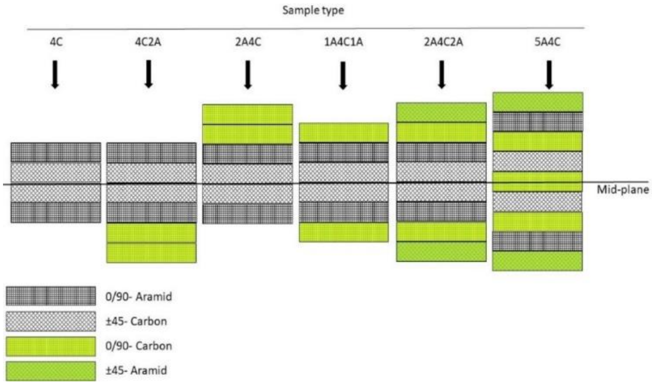

Fig. 1 Sequential details of the specimens (Andrews Zachariah *et al.* 2024)

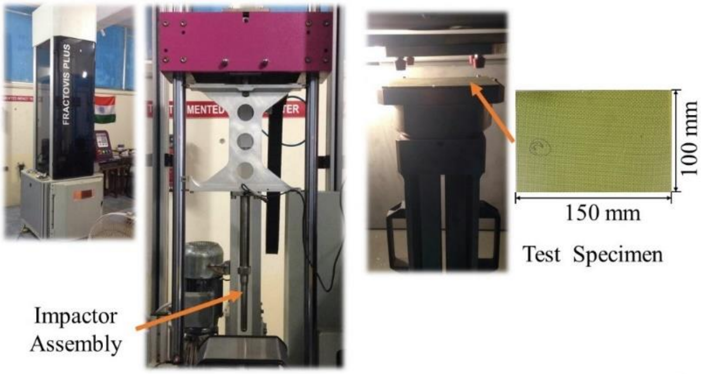

Fig. 2 Drop tower impact setup

Table 1 Physical properties of the sample (Andrews Zachariah *et al.* 2022, Zachariah *et al.* 2021)

Sample Type	Layer	Thickness (mm)	ρ_{exp} (g/cc)	ρ_{th} (g/cc)	Void %	The fraction of aramid fibre
4C	4	1.01	1.42	1.36	4.865	0
4C2A	6	1.66	1.32	1.49	4.901	0.5
2A4C	6	1.66	1.32	1.49	4.901	0.5
1A4C1A	6	1.64	1.33	1.39	4.117	0.5
2A4C2A	8	2.27	1.33	1.39	4.873	1
5A4C	9	2.37	1.32	1.42	4.458	1.25

of the laminates are tabulated in Table 1 (Andrews Zachariah *et al.* 2022, Zachariah *et al.* 2021). Impact test specimens were prepared as per ASTM D7136M - 15, cut using water jet cutting at StoneMax Waterjet & Laser Cutting, Cochin, India.

2.2 Drop weight low-velocity impact

All the specimens were tested using CEAST - FRACTOVIS PLUS drop weight impact test machine at Madras Institute of Technology, Chennai, India, as per ASTM D7136M - 15. Multiple

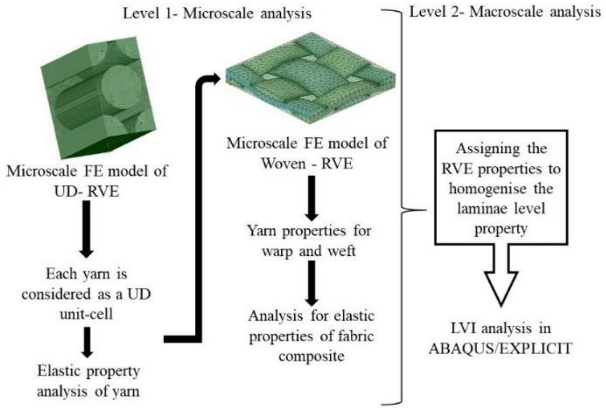

Fig. 3 Schematic of workflow in numerical modelling and simulation (Zachariah *et al.* 2021)

samples of each type of laminate were tested for confirming the repeatability of test data, and the average value of the data is presented. A hemispherical steel impactor with a diameter of 12.7 mm and a mass of 2 kilograms is used for the LVI test, and the test was conducted at a velocity of 3 m/s. The drop heights have been varied to obtain different impact energies. The impact energy E, were chosen based on Eq. (1) for impact energy calculation as per standard ASTM D7136M - 15.

$$E = C_E h \tag{1}$$

Where, C_E indicates the specified ratio of impact energy to specimen thickness and defined as 6.7 J/mm. The two energy ranges studied are 10 J, and 15 J derived based on the thickness of the hybrid laminates. The experimental raw data consisted of the load, displacement, time and energies recorded during the impact event.

2.3 Post- impact damage detection

The damage footprint of the impacted samples was detected using the images obtained from ultrasonic C-Scan. The ultrasonic C-Scan is a widely used Non-destructive test (NDT) for detecting damage footprints in polymer composites (Lin and Waas 2021, Panettieri *et al.* 2016). The scanning image was acquired using Shruti scanning high-resolution ultrasonic testing and imaging equipment manufactured by Dhvani R&D Solutions Pvt Ltd, Chennai, India. Water Coupled through transmission C-Scan was performed for identifying the delamination extend in the impacted samples. The scanning was carried out at a signal frequency of 5 MHz. The C-scan images were acquired using acqUT data acquisition software, and the post image analysis was performed using extUT C-Scan post-processor.

3. Numerical study

3.1 Representative volume element modelling

The numerical modelling and simulation of the LVI test were carried out at two levels, as represented in Fig. 3. The unit cell RVE model generation for microscale property homogenisation

Table 2 Constituent material property for RVE model (Andrews Zachariah *et al.* 2022, Zachariah *et al.* 2021)

Constituent properties	Units	Carbon	Aramid	Epoxy
Density	g/cc	1.81	1.44	1.16
Modulus in X direction	GPa	230	86	3.78
Poisson's ratio v_{xy}		0.25	0.36	0.35
Shear Modulus in XY	GPa	25	3	1.4

was carried out at the first level. The modelling of the RVE was performed in the ANSYS WORKBENCH -Material Designer module (Naghdinasab *et al.* 2018, Rayhan and Rahman 2020). The RVE defines the smallest volume element of a material with an accurate statistical representation of the typical material properties used in a macroscale model. A fibre volume fraction of 0.56 is upheld in the RVE modelling to match it with the experimental data. The RVE approach simulates the microscale behaviour of material systems that consist of distinct constituents or a microstructure. Micro- mesoscale analysis in an RVE provides the homogenised properties for the material microstructure usable in the second-level analysis in ABAQUS/EXPLICIT.

The RVE was modelled following the inbuilt procedure as per the ANSYS Material Designer module with default periodic boundary condition for the UD-RVE and material symmetry in XY for woven RVE. The constituent material properties used for the UD unit cell are obtained from the manufacturer's datasheet, as shown in Table 2.

The elastic properties of the UD unit cell attained from the finite element analysis have been considered the yarn properties in the warp and weft direction to model the microscale unit cell of woven RVE. During the woven unit cell modelling, the fabric thickness of 0.2 mm and 0.3 mm as per the manufacturer data sheet was incorporated. The plain weaving pattern was used to match the experimental sample with a reinforcement volume fraction of 0.56. An appropriate yarn spacing and 0/90 angle for the warp and weft direction was assigned to match the fibre architecture used in the experimental study. The homogenized laminae property derived from the RVE used for macroscale modelling is shown in Table 3.

3.2 Finite element modelling of low-velocity impact

The unit-cell properties obtained through the RVE model analysis have been incorporated as the homogenised laminae properties for the level-2 macroscale analysis. The basic elastic lamina properties used in impact analysis is furnished in Table 3 and were obtained as the result of the analysis of woven RVE (Andrews Zachariah *et al.* 2022, Zachariah *et al.* 2021).

The material damage behaviour is determined based on Hashin damage criteria. Hashin damage criterion is one of the most famous criteria for predicting failure initiation at the lamina level, established in terms of expressions using material strengths (Fischer *et al.* 2019). Hashin failure criteria can predict the four primary modes of damages in laminates at the ply level. The four different failure modes in the Hashin criterion are expressed using Eqs. (2)-(5) as follows

Fibre tensile failure ($\sigma_{11} \geq 0$)

$$F_{ft} = \left(\frac{\sigma_1}{X_T}\right)^2 + \alpha\left(\frac{\sigma_{12}}{S_{12}}\right)^2 + \alpha\left(\frac{\sigma_{13}}{S_{13}}\right)^2 \geq 1 \tag{2}$$

Fibre compression failure ($\sigma_{11} < 0$)

Table 3 Homogenised lamina property for simulation (Andrews Zachariah *et al.* 2022, Zachariah *et al.* 2021)

Properties	Units	Carbon lamina	Aramid lamina
Density	g/cc	1.4	1.24
Modulus in X direction	GPa	38	17
Modulus in Y direction	GPa	38	17
Modulus in Z direction	GPa	7.5	7.2
Poisson's ratio v_{xy}		0.029	0.12
Poisson's ratio v_{yz}		0.47	0.53
Poisson's ratio v_{xz}		0.47	0.53
Shear Modulus in XY	GPa	7.5	7.4
Shear Modulus in YZ	GPa	3	4.2
Shear Modulus in XZ	GPa	3	4.2

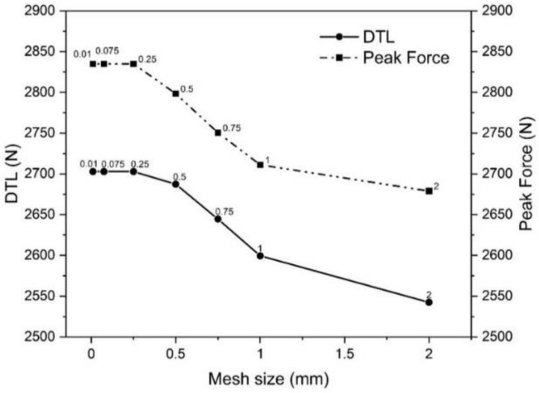

Fig. 4 Mesh convergence plot

$$F_{fc} = \left(\frac{\sigma_1}{X_C}\right)^2 \geq 1 \tag{3}$$

Matrix tensile failure ($\sigma_{22} + \sigma_{33} \geq 0$)

$$F_{mt} = \left(\frac{\sigma_2+\sigma_3}{Y_T}\right)^2 + \left(\frac{1}{S^2{}_{23}}\right)(\sigma_{23}{}^2 - \sigma_{23}\sigma_{33}) + \left(\frac{\sigma_{12}}{S_{12}}\right)^2 + \left(\frac{\sigma_{13}}{S_{13}}\right)^2 \geq 1 \tag{4}$$

Matrix compression failure ($\sigma_{22} + \sigma_{33} < 0$)

$$F_{mc} = \left(\frac{\sigma_2+\sigma_3}{2S_{13}}\right)^2 + \left(\frac{\sigma_2+\sigma_3}{Y_C}\right)\left[\left(\frac{Y_C}{2S_{23}}\right)^2 - 1\right] + \left(\frac{1}{S^2{}_{23}}\right)(\sigma_{23}{}^2 - \sigma_2\sigma_3) + \left(\frac{\sigma_{12}}{S_{12}}\right)^2 + \left(\frac{\sigma_{13}}{S_{13}}\right)^2 \geq 1 \tag{5}$$

In the above equations, X_T and X_C denotes the tensile and compressive strengths in fibre direction; Y_T and Y_C, the tensile and compressive strengths in the transverse direction; S_{12}, S_{13} and S_{23} are the shear strengths, respectively; α is the shear failure coefficient applied to determine the contribution of shear stresses on the fibre tensile failure. σ_i and σ_{ij} are the stresses in longitudinal and transverse directions.

The mesh convergence study for the 2A4C2A sample in the drop tower simulation involved seven

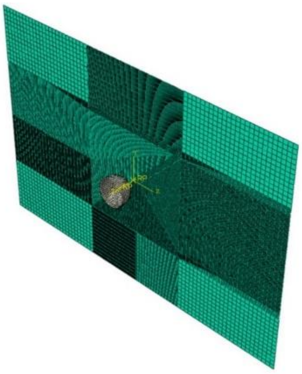

Fig. 5 LVI assembly model for numerical simulation with macroscale laminate design

mesh sizes. Results were compared with experimental data, focusing on Delamination Threshold Load (DTL) and peak force to assess mesh dependency. All meshes maintained an aspect ratio close to 1, with appropriate edge seeding and element thickness. No significant changes in computational time were noted between 0.5 mm and 0.25 mm mesh sizes. A 0.25 mm mesh size was chosen as optimal, as further refinement showed no substantial result variations as shown in Fig. 4.

Numerical simulation of the LVI analysis was performed in FEA package ABAQUS/EXPLICIT. The laminates investigated in the experimental study is modelled using the composite layup extension of the property module. The lamina thickness employed in the model is obtained from the experimental data. As part of confirming the computational accuracy and efficiency, finer mesh with an element size of 0.25 mm derived from the mesh convergence study is applied at the impact zone, and the coarser mesh was allocated outside the impact region. The hemispherical cylindrical impactor with a diameter of 12.7 mm is modelled as a discrete rigid body with a point mass of 2 kg, identical to the experimental setup. The model assembly for LVI simulation is shown in Fig. 5.

3.3 Contact definition and boundary condition

In the FEM, the inbuilt general surface to surface contact is used to define the contact behaviour between the laminate and the impactor. The tangential behaviour with penalty contact algorithm and friction coefficient along with “hard normal” contact behaviour has been established. A pinned boundary condition with rotational freedom was applied at the four edges of the laminate. The impactor hits the laminate surface at the centre with a velocity and kinetic energy similar to the experimental setup. The amplitude corresponding to the impact event duration was provided based on the normalised velocity against the experimental time interval data.

4. Results and discussion

A The impact behaviour of the CFRP and hybrid samples were analysed based on the force-time, force-deformation, and energy-time responses. The critical behaviour investigated was the transition of the impact scenario from supercritical to a subcritical mode where the former is associated with extensive damage, and the latter causes BVID (Bhudolia and Joshi 2018). An evident and significant shift from supercritical to subcritical impact mode was observed in the CFRP to hybrid samples,

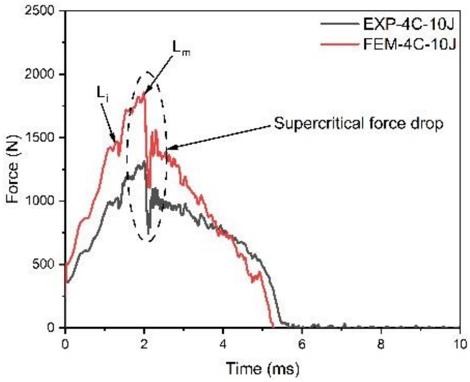

Fig. 6 The force-time response of the 4C sample

respectively. The average experimental data for 10 J and 15 J effects are discussed for ~~a~~ comprehensive analysis of the impact behaviour of the thin carbon/aramid laminates.

4.1 Force -time characteristics

A thorough description regarding the damage initiation, propagation and stiffness degradation can be obtained from the force-time curve at various impact energies. The two prime load points in the force-time variation are the damage initiation load (L_i) and the peak load (L_m), as shown in Fig. 5 (Matadi Boumbimba *et al.* 2017). The trend of the curve until the point L_i is almost linear with fewer fluctuations due to the elastic vibrations caused by Hertzian contact failure. The L_i is the initial point where a primary load drop is observed due to matrix crack and interlaminar delamination. The point L_i, also identified as the delamination threshold load (DTL), the onset of stiffness degradation in the laminate that records the change in specimen compliance. Higher the DTL, the better the damage-resistant (Schoeppner and Abrate 2000). The maximum or peak load L_m for the structure is the load a laminate can withstand before critical damages, including intra-planar fibre breakages and splitting. The higher the value of the L_m, the stiffer the structure is. The force-time curve follows a similar trend for all laminates until the L_i. However, the load re-distribution area represented by the curve to the post DTL illustrates the effectiveness of hybrid strategies employed for impact resistance. After the initial load drop, the failure is depending on the type of laminate.

The CFRP sample 4C, as shown in Fig. 6, underwent a supercritical impact event indicating that the 10 J energy is well above its delamination energy. The laminate exhibited extensive damage with total perforation and the least DTL among the tested samples. The inherent brittle behaviour of the carbon fibre and the epoxy matrix caused brittle damage in the CFRP sample. The rapid force drop after the DTL without a further pickup of the load value indicates extensive damage due to delamination and fibre breakage in the carbon layers followed by a total perforation.

As the aramid fraction is increased from 0 to 0.5 by incorporating two layers of aramid fabric to the 4C configuration, a slight shift from supercritical to subcritical impact is observed, as shown in Figs. 7-9. The load drop in 1A4C1A, 2A4C and 4C2A, nearly resembled the subcritical mode. There was no perforation; instead, a minor penetration observed in 2A4C and 1A4C1A sample. The configuration 4C2A without an aramid layer at the impact side showed comparatively lower peak force. The DTL was very low and was close to 4C laminate, having multiple sawtooth load drops due to the brittle fracture of the carbon layers when directly exposed to impact. The 4C2A had a

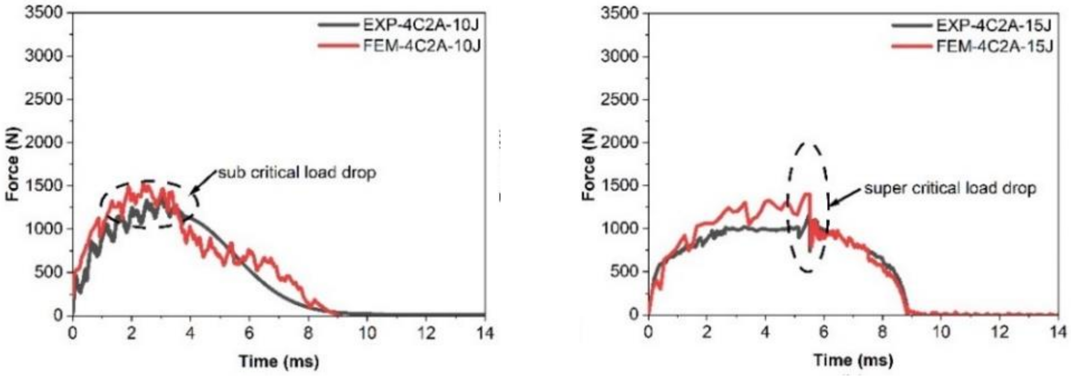

(a) 10 J (b) 15 J

Fig. 7 The force-time curve for 4C2A with 0.5 aramid fraction

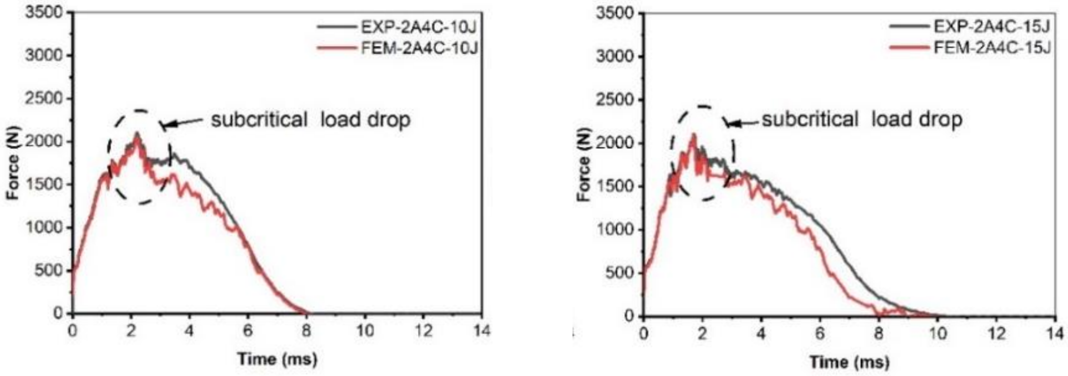

(a) 10 J (b) 15 J

Fig. 8 The force-time curve for 2A4C with 0.5 aramid fraction

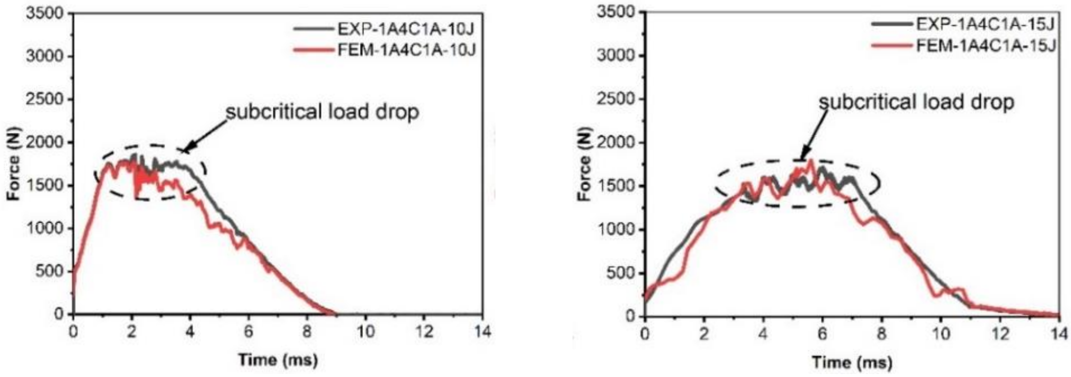

(a) 10 J (b) 15 J

Fig. 9 The force-time response of 1A4C1A sample with single HSM at both sides

nearly supercritical load drop at 10 J impact, as shown in Fig. 7(a). However, it had a through-thickness penetration at 15 J energy impact, as shown in Fig. 7(b).

The 2A4C sample, as shown in Figs. 8(a) and (b), had a marginal increase in the peak force when compared to 1A4C1A, as shown in Figs. 9(a) and (b). The presence of two layers of HSM at the impact side is a reason for improving peak force. However, the DTL and peak force were at the same point for both 2A4C and 1A4C1A, indicating no-load pick up after the initial delamination. Despite the same peak force, at 15 J impact, there was a more considerable sawtooth variation in 2A4C as shown in Fig. 8(b) due to the interlaminar failure in the carbon layers due to the lack of aramid layer at the non-impacted side. However, the samples 2A4C and 4C2A showed an increase in peak load due to the reduced laminate displacement compared to the 4C laminate. The post-peak load section of 4C and 4C2A, as shown in Figs. 6 and 7(a), did not increase the force but a linear behaviour observed due to the lack of the HSM layer and the brittle failure of the subsequent carbon layers. However, the HSM layer at the non-impacted side in 4C2A caused the post-peak section to show a slight climb in the force with a significant saw tooth variation. This variation depicts the toughness and ductility contributed by the HSM layer towards the impact loads.

Nevertheless, the fraction of aramid, the samples, 1A4C1A and 2A4C2A with aramid layers at both the external faces showed a linear behaviour that indicated the aramid HSM layers contributed to taking the further load without extensive damage. The HSM layers placed towards both the outer sides of the laminates could resist the critical damage propagation in the inner carbon laminate.

The load drop in 1A4C1A nearly represented a supercritical nature, as shown in Figs. 9(a) and (b), due to the lack of enough aramid layer at the impact side. However, the aramid layer at the non-impact side significantly resisted the crack growth and fibre breakage, avoiding a through-thickness perforation. The DTL and the peak force were almost similar to a significant plateau region.

The DTL and the peak force for 2A4C2A were significantly improved than 1A4C1A due to the greater number of aramid layers at the top and bottom. However, the top region of the graph in Figs. 10(a) and (b) between the DTL and the start of the unloading portion exhibited a plateau due to the better delamination resistance and crack arresting due to the presence of HSM at both ends. The impact impulse was steadily distributed in the through-thickness direction.

The sample 5A4C with the highest aramid fraction and alternate layers of aramid fabric throughout the laminate sequence exhibited the highest peak force among the samples tested. The resistance to laminate deflection concerning both the projectile deflection and indentation depth has contributed to the high value of peak force. The presence of a larger aramid fraction that resists the laminate deflection is also a reason for the higher peak force observed in 5A4C. The linear peak section of the graph in Figs. 11(a) and (b) with considerably smooth sawtooth variation with minimum intermediate load drops indicates that the 5A4C laminate effectively stopped the propagation of carbon layer failure at 10 J. The presence of alternate HSM layers arrested the brittle damage propagation efficiently. At 15 J impact, the 5A4C sample did not exhibit any significant load pickup after the DTL, which is a clear indication of reaching the threshold energy. The post-peak curve shows many sawtooth variations that indicate the layer by layer delamination in the carbon- aramid interface.

4.2 Force - deformation response

The slope of the curves obtained from the force - deformation plots during ~~an~~ impact shows the laminate stiffness. The force - deformation plots provide the information on maximum deflection damages at various impact energies and the absorbed energy (Abdallah *et al.* 2009). The variations in force from the point of impact till the start of unloading can be analysed as three sections on the deformation scale. The three points into which the entire force variations can be sectioned are the

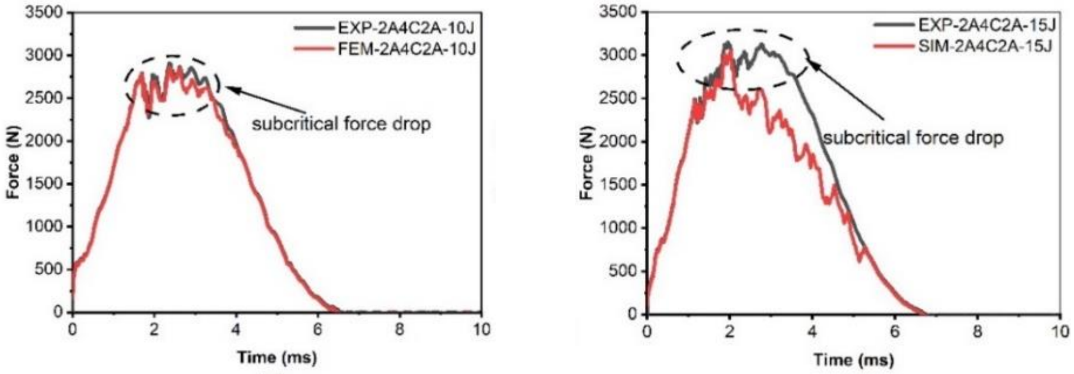

(a) 10 J (b) 15 J

Fig. 10 The force-time response of 2A4C2A sample with two consecutive HSM at both sides

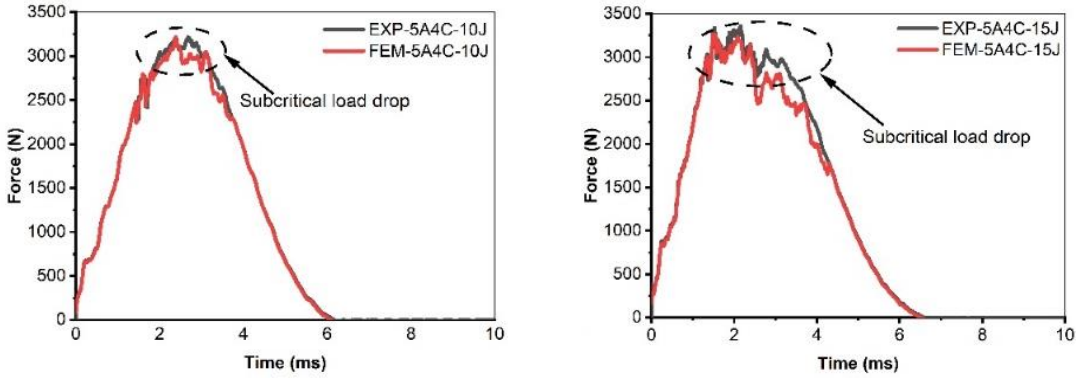

(a) 10 J (b) 15 J

Fig. 11 The force-time response of 5A4C sample with alternate HSM layer

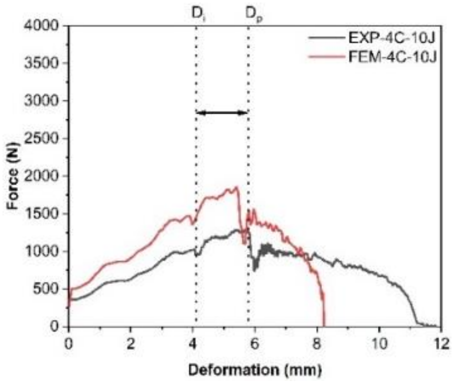

Fig. 12 The force - deformation response of the 4C sample at 10 J

D_i, D_p and D_u, which are the deformations at DTL, peak force and the point at which unloading starts, respectively (Bhudolia and Joshi 2018, Matadi Boumbimba *et al.* 2017), as shown in Fig. 12. As the band between D_p and D_u is less, better is the residual integrity of the laminate. The band

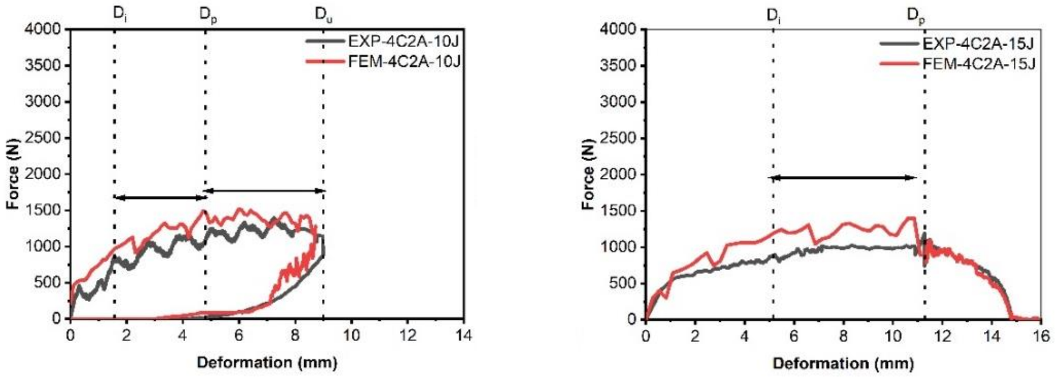

(a) 10 J (b) 15 J

Fig. 13 Force-deformation response of 4C2A with two consecutive HSM at non-impact sides

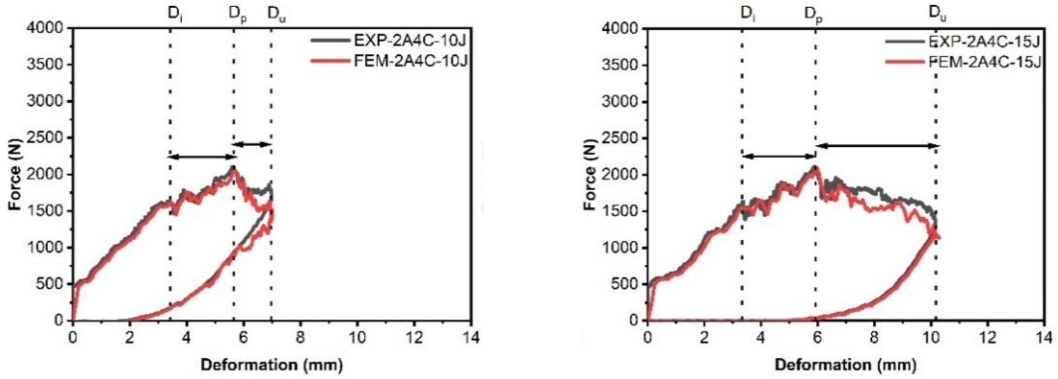

(a) 10 J (b) 15 J

Fig. 14 The force - deformation response of 2A4C with two consecutive HSM at impact sides

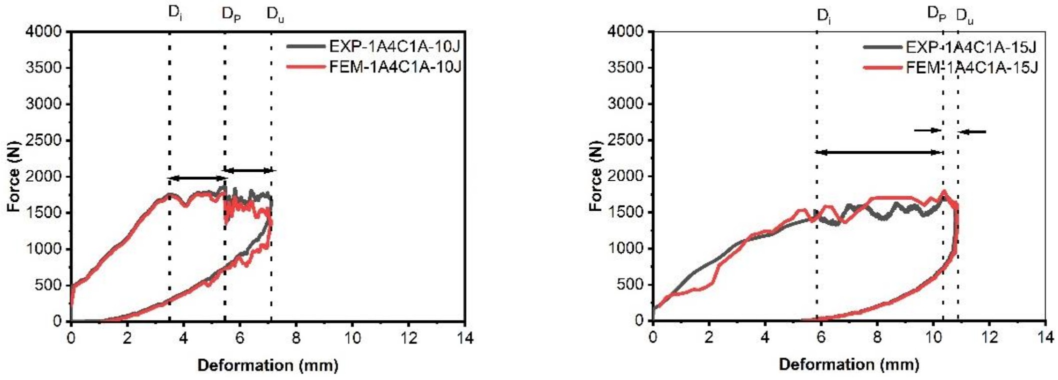

(a) 10 J (b) 15 J

Fig. 15 The force - deformation response of 1A4C1A with single HSM at both sides

between D_i and D_p convey the resistance to damage propagation. Larger the D_i-D_p width, greater is the damage resistance.

Nevertheless, in any stacking sequence or material configuration, the force-deformation curve starts with a pseudo linear phase in response to a monotonic increase in load marking the elastic bending of the laminate. However, the slope of the initial section indicates the stiffness of the laminate (Vieille *et al.* 2013). At 10 J impact energy, CFRP sample 4C, as shown in Fig. 12, has an open-loop curve with the trailing end force slightly above zero, indicating a total perforation. The small force values at the trailing section results from the friction between the tup and the fractured fibre ends (Icten *et al.* 2009).

As a general observation, the initial section of the curve till the DTL for all the hybrid samples exhibited nearly a similar trend. The samples 4C2A, 2A4C and 1A4C1A with 0.5 fractions of the HSM layer had different bandwidth for each section on the curve as shown in Figs. 13, 14 and 15. The plateau region from DTL to the unloading point exhibited similar load drops. This drop is an indication of similar damage propagation that happened in the laminates having carbon fiber laid at its centre.

However, a considerable drop in the force is observed after the DTL until the unloading point due to the degradation in the residual stiffness and the laminate strength. The impact at 15 J on the samples 4C2A, 2A4C and 1A4C1A moved more towards supercritical damage. This shift is a clear indication of reaching the perforation energy for these samples at 15 J, with a significant portion of the total impact energy being absorbed.

The sample 2A4C2A with aramid fraction 1.0 and having ±45° orientation in the hybrid layers above and below the carbon layer exhibited a similar trend at 10 J and 15 J energy levels, as shown in Fig. 16. The plateau region from D_i to D_u was almost linear. However, the sawtooth load drop was observed mainly due to ±45° layup being the crack propagation layer. The 2A4C2A samples rebounded the impactor perfectly without much stiffness reduction. The retention of stiffness is a positive hybrid effect on the through-thickness impact resistance. The presence of ±45° layup for both the carbon and aramid layup facilitated the load pick up at regular intervals during the contact time. At both impact energies, the 2A4C2A sample undergone subcritical damage.

The force - deformation response of 5A4C, as shown in Fig. 17, with an alternate aramid layer to all the 4 carbon layers, exhibited the best impact response among the tested samples, as shown in Fig. 17(a). They had the highest peak force and minimum D_p to D_u bandwidth at10 J. The HSM layers immediate to every carbon layer resisted the immediate stiffness reduction of the entire

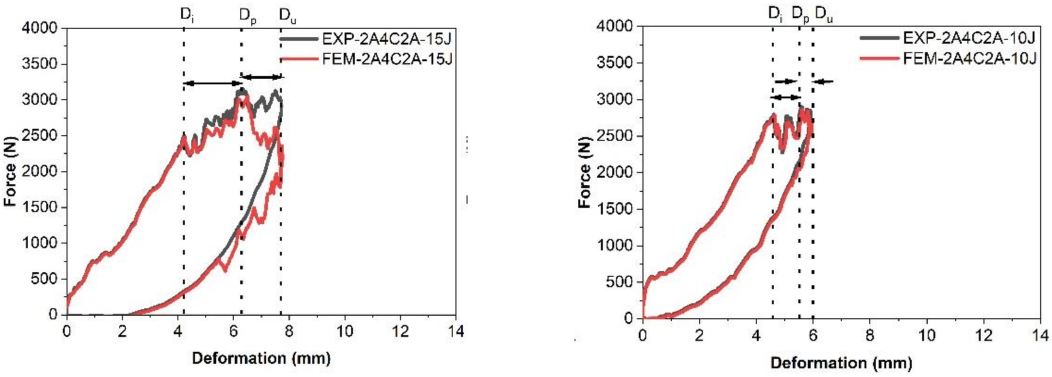

(a) 10 J (b) 15 J

Fig. 16 The force - deformation response of 2A4C2A with two consecutive HSM at both sides

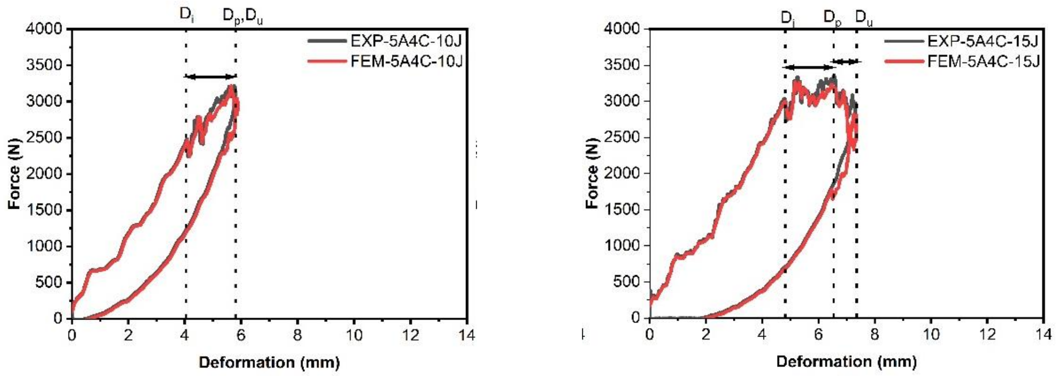

(a) 10 J

(b) 15 J

Fig. 17 The force - deformation response of 5A4C with alternate HSM layer

Table 4 Averaged results of the LVI impact test on hybrid samples

Sample	E_{impact} (J)	Max. displa-cement (mm)	DTL Force (N)	Peak Force (N)	E_{ab} (J)	E_{ab}/E_{impact} (% of energy absorbed)	DI
4C	10	Perforation	360.955±3.17	1311.11±8.45	Perforation	Perforation	0
2A4C	10	6.98±0.03	1634.10±8.06	2098.36±11.23	7.26±0.09	72.65	1.04±0.02
	15	10.08±0.11	1633.49±11.43	2100.20±6.06	13.36±1.02	89.05	0.58±0.02
4C2A	10	8.98±0.05	460.54±5.03	1393.01±18.43	7.77±0.11	77.69	0.96±0.03
	15	Perforation	468.54±6.88	1192.44±9.18	Perforation	Perforation	0
1A4C1A	10	7.19±0.02	1754.60±13.99	1860.71±5.11	7.09±0.05	70.87	1.03±0.05
	15	10.79±0.08	1525.75±19.03	1719.32±9.06	11.04±0.05	73.60	0.84±0.09
2A4C2A	10	5.91±0.02	2795.37±9.41	2895.81±17.78	5.37±0.02	53.67	1.69±0.02
	15	7.71±0.01	2493.41±8.55	3147.38±9.98	10.61±0.07	70.70	1.02±0.04
5A4C	10	5.79±0.03	2480.55±16.53	3216.75±7.09	4.81±0.06	48.13	2.03±0.09
	15	7.31±0.02	3033.62±9.03	3358.84±8.89	10.34±0.13	68.90	1.22±0.08

laminate when the 4C layers face the impact impulse when they are stacked together. However, the ±45° caused the intermediate drops and picked rise for the loads during the entire contact time. At 15 J impact energy, as shown in Fig. 17(b), the force-deflection curve exhibited a wider plateau area and a significant bandwidth between D_p and D_u. This variation indicates a substantial amount of damage propagation from the top to bottom layer.

4.3 Energy - time response

The result analysis in the perspective of energy data can provide informative insights into the distribution of impact energy by different laminates. The primary energy aspects worthy for discussion are the energy absorbed (E_{ab}) out of the total incident energy on the laminate, the energy at the peak load (E_m) identified from the data point at peak load and the ductility index or damage index (DI), which is the dimensionless parameter obtained from the ratio of E_m and E_{ab}. The DI

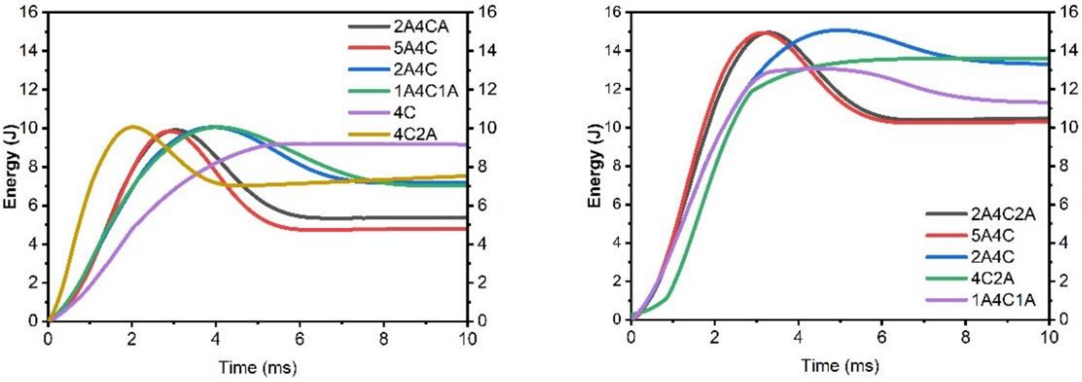

(a) 10 J (b) 15 J

Fig. 18 The energy - time response of tested samples

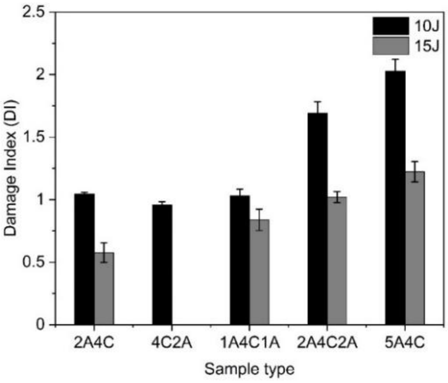

Fig. 19 Damage index plot for the tested samples at different impact energies

reveals the impact fracture toughness and utilisation of total impact energy towards damage initiation and propagation (Ying *et al.* 2017). The energy data represented in Table 4 conveys the energy absorption that happened in the different samples under investigation.

The DI is higher when the material undergoing impact consumes lesser energy through damage propagation due to its significant impact resistance. The energy-time variation of the 4C sample at 10 J behaved differently to the hybrid samples with lower peak energy and no elastic energy. The complete penetration has absorbed the total incident energy. The slope of the initial part of the energy-time curve shows a bi-linearity. As observed in Figs. 18(a) and (b), the initial part of the energy curve shows a similar trend for all the samples. The dent formed due to Hertzian contact and elastic deformation are responsible for this trend. Steep slope in impact energy until the peak value relates deformation and the damage depth.

Sample 4C had the least slope among the samples due to the total perforation. In samples 2A4C and 1A4C1A with aramid fraction 0.5, the slopes at the initial section were similar and were observed to be lesser than the samples 2A4C2A and 5A4C. The elastic deflection added with the damage depth in 2A4C and 1A4C1A has caused the curve to lean more towards the time scale, whereas the samples 2A4C2A and 5A4C had lesser impactor projectile distance through the material. Larger the slope better the integrity of the laminate. The energy-time variation for 2A4C2A

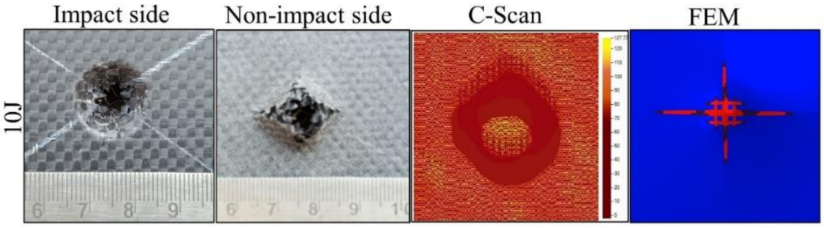

Fig. 20 The post-impact damage profile in the 4C sample

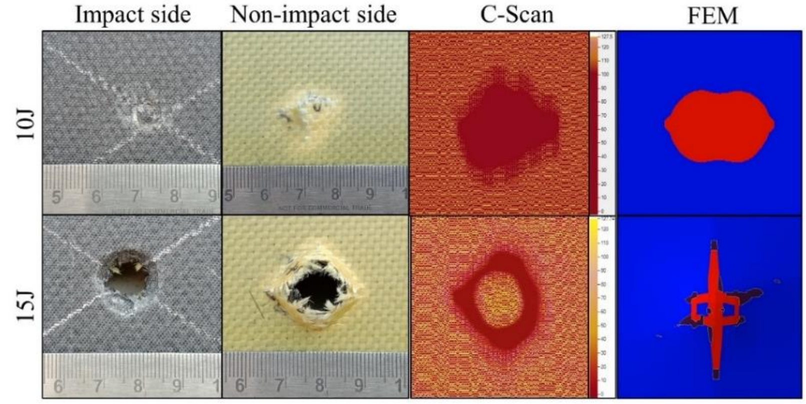

Fig. 21 The post-impact damage profile in the 4C2A sample

and 5A4C was almost similar to the 10 J curve; however, the absorbed energy value of both is very close at 15 J impact, indicating a more extensive damage propagation has occurred 5A4C sample. The DI of the hybrid samples is shown in Fig. 19.

The enhancement and variations of DTL and peak force due to the presence of hybrid HSM layers is presented in Table 4. Samples with Aramid layers at both sides have significantly improved the impact peak force and DTL, indicating an enhancement of impact resistance. The number of layers of HSM had a significant influence on the overall displacement of the laminate. As the number of HSM layers increased, the laminate stiffness improved, causing the samples to deflect the least.

4.4 Damage analysis

The anisotropy and fibre-reinforced composite energy absorption characteristics cause the damages in a laminate to differ significantly between the layers on the surface and at the interior. The damage causing scenario as well matters the internal morphology of the damaged part. Due to the unique wave propagation behaviour of low-velocity impact, the surface may not have apparent visual damage, and its interior may have severe damage due to the absorption of transient impact energy. Therefore, internal damage is an essential factor in evaluating the impact properties of materials.

This study carries the analysis of the damage footprint in the laminate after impact at different energies. Delamination being a prime damage mode in impact loading can vary based on the HSM layer's location and stacking sequence. The C- Scan images illustrated in the study are focused at the centre of the sample with a 40 mm×40 mm window size to quantitatively compare the extent of

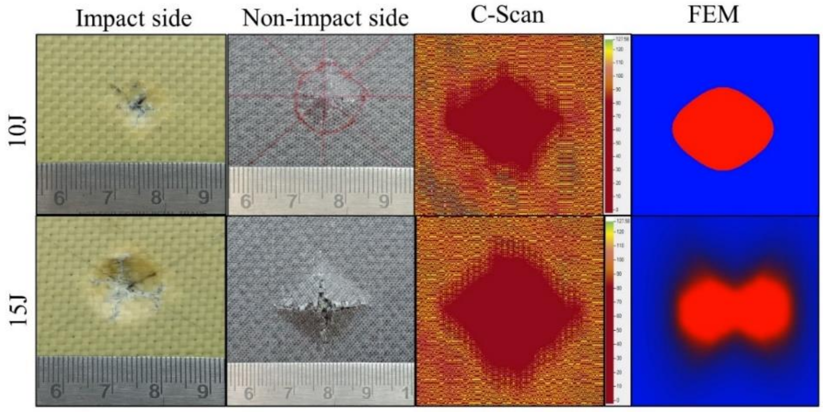

Fig. 22 The post-impact damage profile in the 2A4C sample

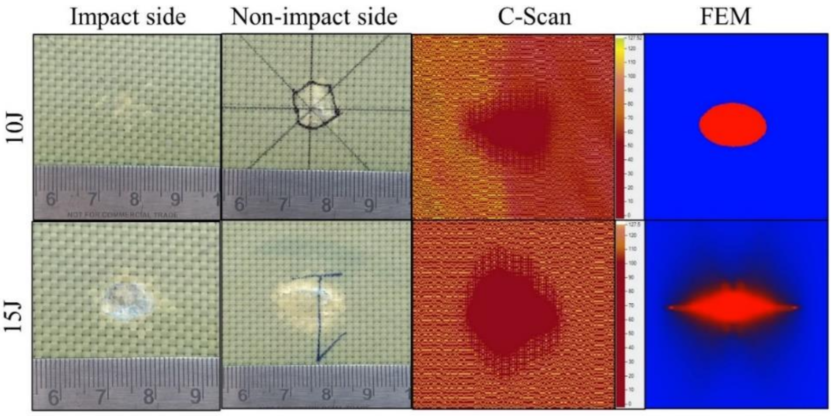

Fig. 23 The post-impact damage profile in the 1A4C1A sample

damage footprint at different energies in various samples. The 4C sample, as shown in Fig. 20, had a minor damage footprint apart from the hole at the centre of impact since the 10 J impact was well above its failure threshold, and the impact went through the thickness, creating a hole with lesser impact wave travelling throughout the interlaminar region.

In all the hybrid samples, the delamination area observed in the C-scan was more compared to the visible damage profile recorded as a camera image. The reason for the increased delamination contour is the BVID at the interlaminar level.

The samples 4C2A at 10 J had an evident perturbation at the non-impacted face, as shown in Fig. 21. However, at 15 J impact energy, the damage in 4C2A resembled 4C with a through-hole. However, the delamination area is more around the hole in 4C2A at 15 J due to the HSM layer's presence.

The damage in 2A4C with two HSM layer only at the impact face had a BVID at the impact side, as shown in Fig. 22. However, the carbon layer has pulled out correctly at the non-impacted side, causing delamination of rhombus contour. The delamination was significant between the aramid - carbon interphase. The delamination contour at both 10 J and 15 J closely resembled the damage profile observed at the non-impact side of the 2A4C laminate.

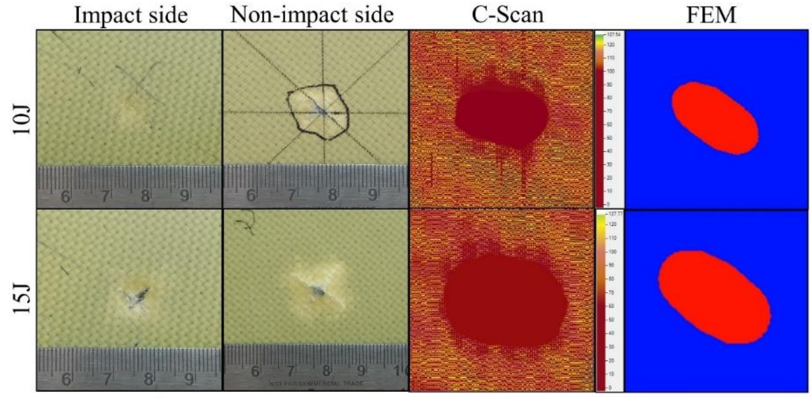

Fig. 24 The post-impact damage profile in the 2A4C2A sample

At 10 J impact, the sample 1A4C1A had a delamination area that is comparatively less as compared to all hybrid sample. The absence of a 45° HSM layer is inferred as the reason behind the fewer delamination spread. However, at 15 J, the sample had severe internal damage due to the less HSM layer at the impact face, as shown in Fig. 23.

Hybrid laminate 2A4C2A, the delamination had an elliptical contour with the major axis inclined at 45°. The presence of ±45 HSM being the stress concentration layer has contributed to the inclination shown in Fig. 24.

The delamination area for 5A4C is, as shown in Fig. 25, observed to be less compared to 2A4C2A. The alternate arrangements of the HSM layer within the carbon layup effectively arrested the delamination propagation. The consecutive HSM layers in 2A4C2A created more stress field, contributing to a larger delamination contour.

5. Numerical validation of results

The composite laminates are impacted at 10 J and 15 J, energy similar conducted in the experimental study. The predictions from numerical simulation were compared with the experimental force-time and force-deflection histories. The implemented Hashin damage model was able to forecast the LVI response with adequate accuracy.

The force-time results are compared with the experimental values in Figs. 6-11. A similar trend between the numerical simulation and experimental data is observed in all the tested energies. However, the numerically predicted force-time histories are slightly varied primarily at the unloading phase compared to experimental plots. The more time required for contact release in the numerical model to make the impactor entirely to its initial condition is attributed as the cause for slightly different behaviour in the unloading regions in the plots. The DTL and peak values of forces are in close accordance with the experimental data.

The force-deflection histories for all the tested scenarios have been numerically simulated. Comparison of the force-deformation obtained through the numerical simulation with the experimental results is shown in Figs. 12-17. The predicted force versus deformation progress was in close accordance with the experimental data from the loading phase until the unloading point D_u. After the contact, the spiky force variation is observed in the unloading curve. However, the

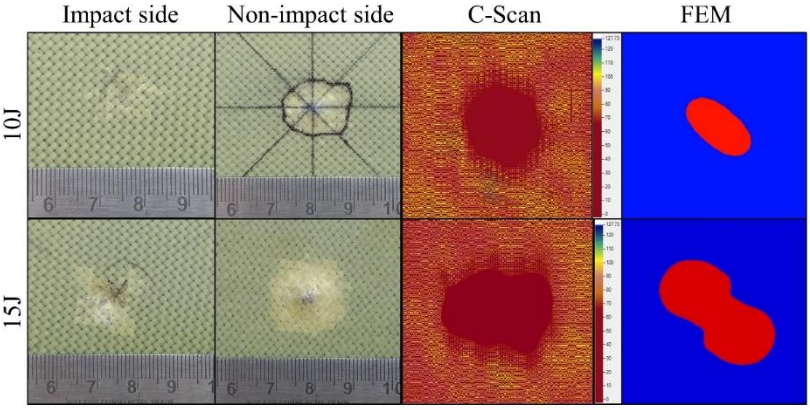

Fig. 25 The post-impact damage profile in the 5A4C sample

maximum deflection is well captured, almost similar to the experimental projectile. Also, the hysteresis is close to the experimental results in all the simulations.

The delamination footprint observed in the FEA results shown in Figs. 20-25 is close to the C-Scan results. The damage footprint in the FEA results is captured with a discrete contour setting with a dual colour spectrum to the effective and exclusive illustration of the damage profile. The FEM post-impact images of the samples 4C and 4C2A at 15 J where through-hole penetration happened during the experimental LVI drop test are shown in Figs. 20 and 21, where the red colour reflects the perforation slit, and the element deletion is identifiable. The overall damage footprint in all the hybrid samples is effectively captured in the FEA using Hashin damage criteria. The inclination of delamination contour and the overall damage profile produced in 2A4C2A, 5A4C, 1A4C1A and 2A4C samples have been closely captured in the FEA images. For impacts at 15 J samples, 1A4C1A, 2A4C, and 4C2A had produced visible perturbations at the non-impacted side, which is not effectively captured in the C-Scan images as there is no through holes. The absence of the hole indication is that the aramid layer has avoided the laminate's total brittle breakage. However, the FEM images for samples 1A4C1A, 2A4C and 4C2A have effectively represented the perturbations as a narrow rhombus with two-sided retracted towards the centre of the laminate representing star or non-convex polygon. In general, the predictions and interpretations derived from the numerical simulation reported is complying the experimental data comprehensively, providing insights into the impact behaviour of hybrid composites. The detailed discussion of the stress- strain curve was not obtained as the output from the RVE analysis in ANSYS Material Designer limits the same. However, it can be proposed as a future opportunity.

6. Conclusions

This study experimentally investigates the behavior of thin woven carbon/aramid hybrid composite laminates, used in mini-UAV structural components, under low-velocity impact loading. The results, validated through numerical simulations based on the RVE model, involve six sample configurations: one CFRP and five hybrid samples with plain-woven aramid fabric in various orientations and locations with plain-woven carbon fiber. Experiments were conducted using a drop tower impactor at 10 J and 15 J impact energies. The data were validated through LVI analysis in ABAQUS/EXPLICIT. The study's significant contributions and findings are as follows:

- The addition of woven fabric aramid hybrid inter-ply layers significantly improved the impact resistance of thin CFRP laminates. The proportion of hybrid layers enhanced overall impact stiffness, damage tolerance (DTL), and peak impact forces. Specifically, hybrid samples with aramid fractions of 0.5 and 1 showed DTL improvements of 360% and 600%, respectively, compared to CFRP. However, sample 4C2A, with a 0.5 aramid fraction but no high-strength material (HSM) on the impact side, did not show a DTL difference from 4C, highlighting the importance of HSM placement. Hybrid samples also exhibited a notable increase in peak load. The inter-ply hybrid approach with HSM fibers can improve through-thickness impact strength and specific weight in thin laminate applications.
- The presence of the HSM layer on both the impact and non-impact faces notably reduces damage footprint and dent perturbation in thin laminates. In samples with HSM layers on both sides, the range of internal damage progression (D_p to D_u) is narrower, resulting in better residual stiffness.
- Hybrid samples absorbed less energy from the incident impact due to the presence of HSM hybrid layers, indicating greater resistance to crack propagation and delamination. All hybrid samples exhibited rebound energy, with 2A4C2A and 5A4C showing the highest levels, making them stronger against impact loads. The quasi-isotropic layup of both carbon and aramid fabric, along with HSM layers on both faces, contributed to their superior performance and moderate damage index (DI) among the samples tested.
- Ultrasonic imaging of post-impact specimens revealed interior delamination associated with barely visible impact damage (BVID). C-Scan images showed that the direction of delamination in laminates with angled fabric layers can be analyzed. Results indicated that alternating HSM layers, as in 5A4C, effectively reduce delamination area. Additionally, the number of layers, stacking angle, and fraction of HSM layers significantly influence the overall damage profile in the LVI behavior of hybrid laminates.
- This study demonstrates that incorporating HSM fabric layers significantly enhances the impact behavior of thin CFRP laminates. The damage index (DI) improved by an average of 110% in specimens with 0.5 fractions of HSM and 185% in those with 1-1.5 fractions. The superior DI and impact strength shown by 5A4C and 2A4C2A indicate that fabric stacking angle, location, and fraction play a crucial role in optimizing the impact performance of thin laminates for mini UAV structural applications.

The RVE-based property homogenization approach used for numerical simulation of LVI on composite laminates validated the experimental investigation. The numerical study's force-time and force-deformation histories closely matched the experimental data. The Hashin damage criteria accurately captured force drops due to damage events, consistent with the experiments. In aerospace applications, minimizing laminate thickness is crucial to avoid adding weight to the structure. Thus, industries seek thin structural composites with tailored properties. This study provides valuable insights for further research into enhancing the impact properties of hybrid composites with various fiber architectures, suitable for thin and lightweight UAV and drone components. Developing thin, robust structures can increase payload capacity and improve instrumentation protection during impacts or crash landings.

Acknowledgements

The authors would like to acknowledge the facility support from the Department of Aeronautical and Automobile Engineering, Manipal Institute of Technology (MIT), MAHE, Manipal.

Funding

This research did not receive any specific grant from funding agencies in the public, commercial, or not-for-profit sectors.

Data availability

The raw/processed data required to reproduce these findings cannot be shared at this time as the data also forms part of an ongoing study.

References

Abdallah, E.A., Bouvet, C., Rivallant, S., Broll, B. and Barrau, J.J. (2009), "Experimental analysis of damage creation and permanent indentation on highly oriented plates", *Compos. Sci. Technol.*, **69** (7-8), 1238-1245. https://doi.org/10.1016/j.compscitech.2009.02.029.

Andrews Zachariah, S., Dayananda, P.K., Padmaraj, N.H. and Shenoy, B.S. (2024), "An analogy of RVE-based numerical model and experimental study of Charpy impact on thin carbon/aramid hybrid composites for micro/mini-Belly landing UAV fuselage", *Cogent Eng.*, **11**(1), 2363465. https://doi.org/10.1080/23311916.2024.2363465.

Andrews Zachariah, S., Satish Shenoy, B., Jayan, J. and Pai, K.D. (2022), "Experimental investigation on dynamic and static transverse behaviour of thin woven Carbon/Aramid hybrid laminates", *J. King Saud Univ. Eng. Sci.*, **34**(4), 273-281. https://doi.org/10.1016/j.jksues.2020.09.015.

ASTM D7136/D7136M (2007), Standard Test Method for Measuring the Damage Resistance of a Fiber-Reinforced Polymer Matrix Composite to a Drop-Weight Impact Event, ASTM International, West Conshohocken, PA, USA.

Bandaru, A.K., Patel, S., Ahmad, S. and Bhatnagar, N. (2018), "An experimental and numerical investigation on the low velocity impact response of thermoplastic hybrid composites", *J. Compos. Mater.*, **52**(7), 877-889. https://doi.org/10.1177/0021998317714043.

Berk, B., Karakuzu, R. and Toksoy, A.K. (2017), "An experimental and numerical investigation on ballistic performance of advanced composites", *J. Compos. Mater.*, **51**(25), 3467-3480. https://doi.org/10.1177/0021998317691810.

Bhudolia, S.K. and Joshi, S.C. (2018), "Low-velocity impact response of carbon fibre composites with novel liquid Methylmethacrylate thermoplastic matrix", *Compos. Struct.*, **203**, 696-708. https://doi.org/10.1016/j.compstruct.2018.07.066.

Bulut, M. and Erkliğ, A. (2018), "An experimental investigation on damage characteristics of laminated hybrid composites subjected to low velocity impact", *Polym. Compos.*, **39**(9), 3129-3139. https://doi.org/10.1002/pc.24319.

Condruz, M.R., Paraschiv, A., Deutschlander, A. and Mîndru, I. (2020), "Assessment of GFRP mechanical properties in order to determinate suitability for UAV components", *Key Eng. Mater.*, **834**, 57-66. https://doi.org/10.4028/www.scientific.net/KEM.834.57.

Denning, K. (2004), "Design, construction, and testing of a high-speed, light-weighted UAV", *AIAA 3rd "Unmanned Unlimited" Technical Conference, Workshop and Exhibit*, Chicago, IL, USA, September.

Dixit, A., Mali, H.S. and Misra, R.K. (2013), "Unit cell model of woven fabric textile composite for multiscale analysis", *Procedia Eng.*, **68**, 352-358. https://doi.org/10.1016/j.proeng.2013.12.191.

Dong, Z. and Sun, C.T. (2009), "Testing and modeling of yarn pull-out in plain woven Kevlar fabrics", *Compos. Part A: Appl. Sci. Manuf.*, **40**(12), 1863-1869. https://doi.org/10.1016/j.compositesa.2009.04.019.

Evci, C. and Gülgeç, M. (2012), "An experimental investigation on the impact response of composite materials", *Int. J. Impact Eng.*, **43**, 40-51. https://doi.org/10.1016/j.ijimpeng.2011.11.009.

Fischer, B., Sarasini, F., Tirillò, J., Touchard, F., Chocinski-Arnault, L., Mellier, D., Panzer, N., Sommerhuber, R., Russo, P., Papa, I., Lopresto, V. and Ecault, R. (2019), "Impact damage assessment in biocomposites by micro-CT and innovative air-coupled detection of laser-generated ultrasound", *Compos. Struct.*, **210**, 922-931. https://doi.org/10.1016/j.compstruct.2018.12.013.

Fotouhi, M., Jalalvand, M. and Wisnom, M.R. (2017), "High performance quasi-isotropic thin-ply carbon/glass hybrid composites with pseudo-ductile behaviour in all fibre orientations", *Compos. Sci. Technol.*, **152**, 101-110. https://doi.org/10.1016/j.compscitech.2017.08.024.

Gustin, J., Joneson, A., Mahinfalah, M. and Stone, J. (2005), "Low velocity impact of combination Kevlar/carbon fiber sandwich composites", *Compos. Struct.*, **69**(4), 396-406. https://doi.org/10.1016/j.compstruct.2004.07.020.

Hashim, N., Majid, D.L., Uda, N., Zahari, R. and Yidris, N. (2017), "Vacuum infusion method for woven carbon/Kevlar reinforced hybrid composite", *IOP Conf. Ser.: Mater. Sci. Eng.*, **270**, 012021. https://doi.org/10.1088/1757-899X/270/1/012021.

Huang, C., Cui, L., Liu, Y., Xia, H., Qiu, Y. and Ni, Q.Q. (2021), "Low-velocity drop weight impact behavior of Twaron® fabric investigated using experimental and numerical simulations", *Int. J. Impact Eng.*, **149**, 103796. https://doi.org/10.1016/j.ijimpeng.2020.103796.

Icten, B.M., Atas, C., Aktas, M. and Karakuzu, R. (2009), "Low temperature effect on impact response of quasi-isotropic glass/epoxy laminated plates", *Compos. Struct.*, **91**(3), 318-323. https://doi.org/10.1016/j.compstruct.2009.05.010.

Karahan, M. and Karahan, N. (2014), "Effect of weaving structure and hybridization on the low-velocity impact behavior of woven carbon-epoxy composites", *Fibres Text. East. Eur.*, **22**(3), 109-115.

Karahan, M. and Yildirim, K. (2015), "Low velocity impact behaviour of aramid and UHMWPE composites", *Fibres Text. East. Eur.*, **23**(3), 97-105. https://doi.org/10.5604/12303666.1152522.

Karahan, M., Karahan, N., Nasir, M.A. and Nawab, Y. (2019), "Effect of structural hybridization on ballistic performance of aramid fabrics", *J. Thermoplast. Compos. Mater.*, **32**(6), 795-814. https://doi.org/10.1177/0892705718780197.

Katnam, K.B., Dalfi, H. and Potluri, P. (2019), "Towards balancing in-plane mechanical properties and impact damage tolerance of composite laminates using quasi-UD woven fabrics with hybrid warp yarns", *Compos. Struct.*, **225**, 111083. https://doi.org/10.1016/j.compstruct.2019.111083.

Kumar Jha, A., Sathyamoorthy, S. and Prakash, V. (2019), "Bird strike damage and analysis of UAV's airframe", *Procedia Struct. Integr.*, **14,** 416-428. https://doi.org/10.1016/j.prostr.2019.05.051.

Lin, S. and Waas, A.M. (2021), "Accelerating computational analyses of low velocity impact and compression after impact of laminated composite materials", *Compos. Struct.*, **260**, 113456. https://doi.org/10.1016/j.compstruct.2020.113456.

Mahmoud, B., Manseri, L., Rogani, A., Navarro, P., Marguet, S., Ferrero, J.F. and Tawk, I. (2019), "Experimental and numerical study of the damage mechanisms in hybrid unidirectional/woven composites under impact loading", *Compos. Struct.*, **209**, 606-615. https://doi.org/10.1016/j.compstruct.2018.10.098.

Marom, G., Drukker, E., Weinberg, A. and Banbaji, J. (1986), "Impact behaviour of carbon/Kevlar hybrid composites", *Compos.*, **17**(2), 150-153. https://doi.org/10.1016/0010-4361(86)90253-3.

Matadi Boumbimba, R., Coulibaly, M., Khabouchi, A., Kinvi-Dossou, G., Bonfoh, N. and Gerard, P. (2017), "Glass fibres reinforced acrylic thermoplastic resin-based tri-block copolymers composites: Low velocity impact response at various temperatures", *Compos. Struct.*, **160**, 939-951. https://doi.org/10.1016/j.compstruct.2016.10.127.

Micheli, D., Vricella, A., Pastore, R., Delfini, A., Giusti, A., Albano, M., Marchetti, M., Moglie, F. and Primiani, V.M. (2016), "Ballistic and electromagnetic shielding behaviour of multifunctional Kevlar fiber reinforced epoxy composites modified by carbon nanotubes", *Carbon*, **104**, 141-156.

https://doi.org/10.1016/j.carbon.2016.03.059.

Naghdinasab, M., Farrokhabadi, A. and Madadi, H. (2018), "A numerical method to evaluate the material properties degradation in composite RVEs due to fiber-matrix debonding and induced matrix cracking", *Finite Elem. Anal. Des.*, **146**, 84-95. https://doi.org/10.1016/j.finel.2018.04.008.

Naik, N.K., Chandra Sekher, Y. and Meduri, S. (2000), "Damage in woven-fabric composites subjected to low-velocity impact", *Compos. Sci. Technol.*, **60**(5), 731-744. https://doi.org/10.1016/S0266-3538(99)00183-9.

Nayak, S.Y., Shenoy, S., Hameed Sultan, M.T., Kini, C.R., Seth, A., Prabhu, S. and Safri, S.N.A. (2021), "Effect of CNT-based resin modification on the mechanical properties of polymer composites", *Front. Mater.*, **7**, 609010. https://doi.org/10.3389/fmats.2020.609010.

Nugroho, G., Pranoto, I. and Rohmana, N.Z. (2018), "Effect of breather type and vacuum pressure on the manufacturing of an unmanned aerial vehicle fuselage using vacuum bagging method", *AIP Conf. Proc.*, **1983**(1), 040005. https://doi.org/10.1063/1.5046262.

Padmaraj, N.H., Vijaya, K.M. and Dayananda, P. (2021), "Experimental investigation on fatigue behaviour of glass/epoxy quasi-isotropic laminate composites under different ageing conditions", *Int. J. Fatigue*, **143**, 105992. https://doi.org/10.1016/j.ijfatigue.2020.105992.

Panettieri, E., Fanteria, D., Montemurro, M. and Froustey, C. (2016), "Low-velocity impact tests on carbon/epoxy composite laminates: A benchmark study", *Compos. Part B: Eng.*, **107**, 9-21. https://doi.org/10.1016/j.compositesb.2016.09.057.

Papakaliatakis, G. and Karalekas, D. (2010), "Damage growth by debonding in a single fibre metal matrix composite: Elastoplasticity and strain energy density criterion", *Theoret. Appl. Fract. Mech.*, **53**(2), 152-157. https://doi.org/10.1016/j.tafmec.2010.03.005.

Pigazzini, M.S., Bazilevs, Y., Ellison, A. and Kim, H. (2018), "Isogeometric analysis for simulation of progressive damage in composite laminates", *J. Compo. Mater.*, **52**(25), 3471-3489. https://doi.org/10.1177/0021998318770723.

Priyanka, P., Dixit, A. and Mali, H. S. (2017), "high-strength hybrid textile composites with carbon, kevlar, and e-glass fibers for impact-resistant structures: A review", *Mech. Compos. Mater.*, **53**(5), 685-704. https://doi.org/10.1007/s11029-017-9696-2.

PS, R. and Jeyan, M.L. (2020), "Mini unmanned aerial systems (UAV) - A review of the parameters for classification of a mini UAV", *Int. J. Aviat. Aeronaut. Aerosp.*, **7**(3), 5. https://doi.org/10.15394/ijaaa.2020.1503.

Rayhan, S.B. and Rahman, M.M. (2020), "Modeling elastic properties of unidirectional composite materials using ansys material designer", *Procedia Struct. Integr.*, **28**, 1892-1900. https://doi.org/10.1016/j.prostr.2020.11.012.

Sarasini, F. (2017), "Low-velocity impact behaviour of hybrid composites", *Hybrid Polymer Composite Materials*, Woodhead Publishing, Cambridge, UK.

Schoeppner, G.A. and Abrate, S. (2000), "Delamination threshold loads for low velocity impact on composite laminates", *Compos. Part A: Appl. Sci. Manuf.*, **31**(9), 903-915. https://doi.org/10.1016/S1359-835X(00)00061-0.

Shaker, K., Jabbar, A., Karahan, M., Karahan, N. and Nawab, Y. (2017), "Study of dynamic compressive behaviour of aramid and ultrahigh molecular weight polyethylene composites using Split Hopkinson Pressure Bar", *J. Compos. Mater.*, **51**(1), 81-94. https://doi.org/10.1177/002199831663524.

Shi, Y., Swait, T. and Soutis, C. (2012), "Modelling damage evolution in composite laminates subjected to low velocity impact", *Compos. Struct.*, **94**(9), 2902-2913. https://doi.org/10.1016/j.compstruct.2012.03.039.

Soetanto, M.F. and Tritjahjono, R.I. (2016), "Study the strength of material and composite structures of belly-landing mini UAV", *Appl. Mech. Mater.*, **842**, 178-185. https://doi.org/10.4028/www.scientific.net/AMM.842.178.

Soliman, E.M., Sheyka, M.P. and Taha, M.R. (2012), "Low-velocity impact of thin woven carbon fabric composites incorporating multi-walled carbon nanotubes", *Int. J. Impact Eng.*, **47**, 39-47. https://doi.org/10.1016/j.ijimpeng.2012.03.002.

Sørensen, B.F. (2017), "Micromechanical model of the single fiber fragmentation test", *Mech. Mater.*, **104**, 38-48. https://doi.org/10.1016/j.mechmat.2016.10.002.

Sun, X.C. and Hallett, S.R. (2017), "Barely visible impact damage in scaled composite laminates: Experiments and numerical simulations", *Int. J. Impact Eng.*, **109**, 178-195. https://doi.org/10.1016/j.ijimpeng.2017.06.008.

Troiani, E., Falaschetti, M.P., Taddia, S. and Ceruti, A. (2015), "CFRP crash absorbers in small UAV: Design and optimization", SAE Technical Paper No. 2015-01-2461; SAE International, Warrendale, PA, USA.

Vachon, P.L., Brailovski, V. and Terriault, P. (2013), "Impact-induced damage and damage propagation under flexural load in TiNi and Kevlar-stitched carbon/epoxy laminates", *Compos. Struct.*, **100**, 424-435. https://doi.org/10.1016/j.compstruct.2013.01.011.

Valença, S.L., Griza, S., de Oliveira, V.G., Sussuchi, E.M. and de Cunha, F.G.C. (2015), "Evaluation of the mechanical behavior of epoxy composite reinforced with Kevlar plain fabric and glass/Kevlar hybrid fabric", *Compos. Part B: Eng.*, **70**, 1-8. https://doi.org/10.1016/j.compositesb.2014.09.040.

van Oosterom, S., Allen, T., Battley, M. and Bickerton, S. (2019), "An objective comparison of common vacuum assisted resin infusion processes", *Compos. Part A: Appl. Sci. Manuf.*, **125**, 105528. https://doi.org/10.1016/j.compositesa.2019.105528.

Verma, A.K., Pradhan, N.K., Nehra, R. and Prateek (2018), "Challenge and advantage of materials in design and fabrication of composite UAV", *IOP Conf. Ser.: Mater. Sci. Eng.*, **455**(1), 012005. https://doi.org/10.1088/1757-899X/455/1/012005.

Vieille, B., Casado, V.M. and Bouvet, C. (2013), "About the impact behavior of woven-ply carbon fiber-reinforced thermoplastic- and thermosetting-composites: A comparative study", *Compos. Struct.*, **101**, 9-21. https://doi.org/10.1016/j.compstruct.2013.01.025.

Yang, B., Wang, Z., Zhou, L., Zhang, J. and Liang, W. (2015), "Experimental and numerical investigation of interply hybrid composites based on woven fabrics and PCBT resin subjected to low-velocity impact", *Compos. Struct.*, **132**, 464-476. https://doi.org/10.1016/j.compstruct.2015.05.069.

Yang, S., Chalivendra, V.B. and Kim, Y.K. (2017), "Fracture and impact characterization of novel auxetic Kevlar®/Epoxy laminated composites", *Compos. Struct.*, **168**, 120-129. https://doi.org/10.1016/j.compstruct.2017.02.034.

Ying, S., Mengyun, T., Zhijun, R., Baohui, S. and Li, C. (2017), "An experimental investigation on the low-velocity impact response of carbon-aramid/epoxy hybrid composite laminates", *J. Reinforced Plast. Compos.*, **36**(6), 422-434. https://doi.org/10.1177/0731684416680893.

Zachariah, S., Shenoy, S. and Pai, D. (2024), "Experimental analysis of the effect of the woven aramid fabric on the strain to failure behavior of plain weaved carbon/aramid hybrid laminates", *Facta Univ. Ser.: Mech. Eng.*, **22**(1), 13-24. https://doi.org/10.22190/FUME200819022Z.

Zachariah, S.A., Shenoy, B.S. and Pai, K.D. (2021), "Comprehensive analysis of in-plane tensile characteristics of thin carbon/aramid hybrid composites using experimental and RVE- based numerical study", *Compos. Struct.*, **271**, 114160. https://doi.org/10.1016/j.compstruct.2021.114160.

Zahran, M. and Abdelwahab, M. (2019), "Crash analysis of UAV hybrid composite fuselage structure under different impact conditions", *Mater. Sci. Forum*, **953**, 88-94. https://doi.org/10.4028/www.scientific.net/MSF.953.88.

CC